Ann Nucl Med (2012) 26:319–326
DOI 10.1007/s12149-012-0573-8

ORIGINAL ARTICLE

Usefulness of extent analysis for statistical parametric mapping with asymmetry index using inter-ictal FGD-PET in mesial temporal lobe epilepsy

Tsutomu Soma · Toshimitsu Momose · Miwako Takahashi · Keitraro Koyama · Kensuke Kawai · Kenya Murase · Kuni Ohtomo

Received: 19 October 2011 / Accepted: 15 January 2012 / Published online: 8 February 2012

Abstract
Objective Inter-ictal ^{18}F-2-fluoro-deoxy-D-glucose-positron emission tomography (FDG-PET) is widely used for preoperative evaluation to identify epileptogenic zones in patients with temporal lobe epilepsy. In this study, we combined statistical parametric mapping (SPM) with the asymmetry index and volume-of-interest (VOI) based extent analysis employing preoperative FDG-PET in unilateral mesial temporal lobe epilepsy (MTLE) patients. We also evaluated the detection utility of these techniques for automated identification of abnormalities in the unilateral hippocampal area later confirmed to be epileptogenic zones by surgical treatment and subsequent good seizure control.
Methods FDG-PET scans of 17 patients (9 males, mean age 35 years, age range 16–60 years) were retrospectively analyzed. All patients had been preoperatively diagnosed with unilateral MTLE. The surgical outcomes of all patients were Engel class 1A or 1B with postoperative follow-up of 2 years. FDG-PET images were spatially normalized and smoothed. After two voxel-value adjustments, one employing the asymmetry index and the other global normalization, had been applied to the images separately, voxel-based statistical comparisons were performed with 20 controls. Peak analysis and extent analysis in the VOI in the parahippocampal gyrus were conducted for SPM. For the extent analysis, a receiver operating characteristic (ROC) curve was devised to calculate the area under the curve and to determine the optimal threshold of extent.
Results The accuracy of the method employing the asymmetry index was better than that of the global normalization method for both the peak and the extent analysis. The ROC analysis results, for the extent analysis, yielded an area under the curve of 0.971, such that the accuracy and optimal extent threshold of judgment were 92 and 32.9%, respectively.
Conclusion Statistical *z*-score mapping with the asymmetry index was more sensitive for detecting regional glucose hypometabolism and more accurate for identifying the side harboring the epileptogenic zone using inter-ictal FDG-PET in unilateral MTLE than *z*-score mapping with global normalization. Moreover, the automated determination of the side with the epileptogenic zone in unilateral MTLE showed improved accuracy when the combination of SPM with the asymmetry index and extent analysis was applied based on the VOI in the parahippocampal gyrus.

Keywords Asymmetry index · Statistical parametric mapping · FDG-PET · Mesial temporal lobe epilepsy

T. Soma · T. Momose (✉) · M. Takahashi · K. Koyama · K. Ohtomo
Department of Radiology, Graduate School of Medicine, University of Tokyo, 3-1 Hongo 7-Chome, Bunkyo-ku, Tokyo 113-8655, Japan
e-mail: tmomo-tky@umin.ac.jp

T. Soma · K. Murase
Course of Health Science, Division of Medical Technology and Science, Department of Medical Physics and Engineering, Graduate School of Medicine, Osaka University, Osaka, Japan

T. Soma
Software Development Group, Product Management and Marketing Department, FUJIFILM RI Pharma Co., Ltd, Tokyo, Japan

K. Kawai
Department of Neurosurgery, Graduate School of Medicine, University of Tokyo, Tokyo, Japan

Introduction

Epilepsy surgery has been established as an effective treatment for patients with refractory temporal lobe epilepsy (TLE) [1, 2]. For successful surgical treatment, preoperative lateralization or localization of the epileptogenic zone (EZ) is important. Inter-ictal ^{18}F-2-fluoro-deoxy-D-glucose (FDG) positron emission tomography (PET) is a widely used preoperative method of identifying the EZ. On inter-ictal FDG-PET, areas with metabolic alterations, probably related to epileptogenicity, show decreased FDG accumulation, and these findings of altered metabolism contribute to EZ detection. In preoperative evaluation with inter-ictal FDG-PET, FDG distributions are generally evaluated by visual inspection. However, visual inspection is inevitably associated with inter-observer variation and it is usually difficult to provide numerical values, such as the most appropriate threshold for diagnosis, or statistical parameters derived from comparisons with controls. Therefore, objective semi-quantitative analysis has been anticipated as a method complementing visual evaluation.

Objective semi-quantitative analysis with the region-of-interested (ROI) technique or voxel-based statistical parametric mapping [SPM; Wellcome Department of Cognitive Neurology, London, UK (http://www.fil.ion.ucl.ac.uk/spm/)] has been demonstrated to have utility for preoperative detection of EZ [3–6]. In addition to these methods, some studies incorporated inter-hemispheric asymmetries, such as left to right subtraction, or the asymmetry index (AI), and showed improvement of preoperative evaluations for TLE; however, in most such studies, inter-hemispheric asymmetry was calculated from the mean ROI value or the volume-of-interest (VOI) [7–9]. Few studies have applied asymmetries to voxel-based analysis. Bogaert et al. [10] prepared brain FDG-PET and mirror-reversed images of a patient, and compared them with those of normal controls by SPM. An ^{18}F-4-(2′-methoxyphenyl)-1-[2′-(*N*-2-pyridinyl)-*p*-fluorobenzamido]-ethyl-*p*iperazine PET study demonstrated improved localization of EZ using AI calculated for each voxel, probably because the broad range of variation across normal controls was decreased using AI [11].

In this study, we calculated voxel-based AI images with FDG-PET of unilateral mesial temporal lobe epilepsy (MTLE) patients and compared them with those of normal controls, i.e., we conducted SPM employing AI. With this method, the most significant voxel in the hippocampal area on either side was identified (peak analysis). In addition, we combined the AI-SPM with VOI-based extent analysis, in which we estimated the number of voxels exceeding a threshold, because the EZ is often associated with an extensive area of hypometabolism. These methods were designed to allow automatic processing to provide objective assessments. Then, we applied these methods to preoperative FDG-PET in patients who were candidates for epilepsy surgery, and evaluated the detection utility of these methods for identifying abnormalities in the unilateral hippocampal area later confirmed to harbor the EZ by surgical treatment and subsequent good seizure control. We also compared the diagnostic accuracy of our methods with that of the conventional global normalization (GN) method, employing SPM.

Materials and methods

Patients and controls

FDG-PET for epilepsy evaluation was performed in 145 patients between 2003 and 2009. Among these patients, 51 underwent surgical treatment of the unilateral hippocampal area, and we selected 17 of these patients (9 males, mean age 35 years, range 16–60 years) for this study based on the following inclusion criteria; (1) good postoperative outcome, corresponding to Engel's classification 1A or 1B [12] for more than 2 years; (2) preoperative evaluations including inter-ictal EEG, MRI and inter-ictal FDG-PET had been performed. All preoperative examinations were performed as part of routine evaluations for patients with medically refractory epilepsy who were candidates for epilepsy surgery. Exclusion criteria for this study were; (1) a history of previous cranial surgery, (2) space occupying lesion exceeding 1 cm on MRI; (3) a history of encephalomyelitis. We selected patients with good postoperative outcomes because the EZ was confirmed only by seizure disappearance after surgical treatment of EZ.

The control group of FDG-PET was obtained employing an identical protocol for 20 normal controls (11 males, mean age 47 years, range 24–60 years), who had no neurological or mental diseases, and no history of taking psychotropic drugs.

This retrospective study was performed according to the guidelines of the Ethical Review Board of Tokyo University Hospital. Written informed consent was obtained from all patients and controls. We also obtained permission to analyze the clinical data.

FDG-PET procedure

The patients fasted for at least 5 h and then underwent FDG-PET scanning. A 296 MBq dose of FDG was injected intravenously, and 45 min later, emission scans were obtained in two-dimensional mode for 10 min, and transmission scans were subsequently obtained to correct for photon attenuation using a 68Ga/68Ge rotating rod source.

The PET scanner was an Advance NXi (General Electric Medical Systems), with 12096 bismuth-germanate crystals arranged in 18 rings and a 15.2 cm axial field-of-view. The scanner has an intrinsic spatial resolution in the center of the field-of-view of 4.8 mm full width of half maximum (FWHM) and an axial resolution of 4.0 mm FWHM.

During the examination, the patient rested in the supine position with an eye mask to minimize the confounding factor of environmental noises, and was observed to exclude clinical seizure activity. During the scan, the patient's head was kept in the head holder, and when the head moved, a radiology technician corrected the movement according to a mark on the patient's head and a laser pointer device. The FDG-PET data were reconstructed with ordered subset expectation maximization iterative reconstruction, with 2 iterations and 28 subsets. An 8-mm FWHM Gaussian filter was applied to the image. The data were collected for 37 transaxial slices of a 128 × 128 matrix, with a pixel size of 2.03 × 2.03 mm, and 35 successive slices were separated by 4.25 mm.

^{18}F was synthesized using the Cypris Model 370 Cyclotron (Sumitomo Heavy Industries), and FDG was generated with an automated FDG synthesis system (F100: Sumitomo Heavy Industries) on the day of each scan. Radiochemical purity was greater than 95%.

Data analysis

Data analysis was performed using SPM8 and MATLAB version R2011a (MathWorks Inc., Natick, MA, USA). We used MATLAB for SPM8, and to calculate a statistical value for each voxel on images pre-processed by SPM8.

The data analysis steps were: (1) spatial normalization; (2) smoothing; (3) voxel-value adjustment; (4) *z*-score mapping; (5) peak analysis with *z*-score mapping; and (6) extent analysis with *z*-score mapping (Fig. 1). Further details of each step are presented below.

Spatial normalization and smoothing

All FDG-PET images (17 MTLE patients and 20 controls) were spatially normalized to a standardized stereotactic Montreal Neurological Institute (MNI) space [13] based on the Talairach and Tournoux atlas [14], using 12-parameter linear affine normalization and another 16 nonlinear iteration algorithms with our in-house FDG template. The in-house FDG template was created as follows. First, the 20 control group images were spatially normalized with an FDG template which had been provided by the National Center Hospital for Mental, Nervous and Muscular Disorders [15] using the same parameter as described above. Second, the 20 normalized images were averaged, and a flipped image was

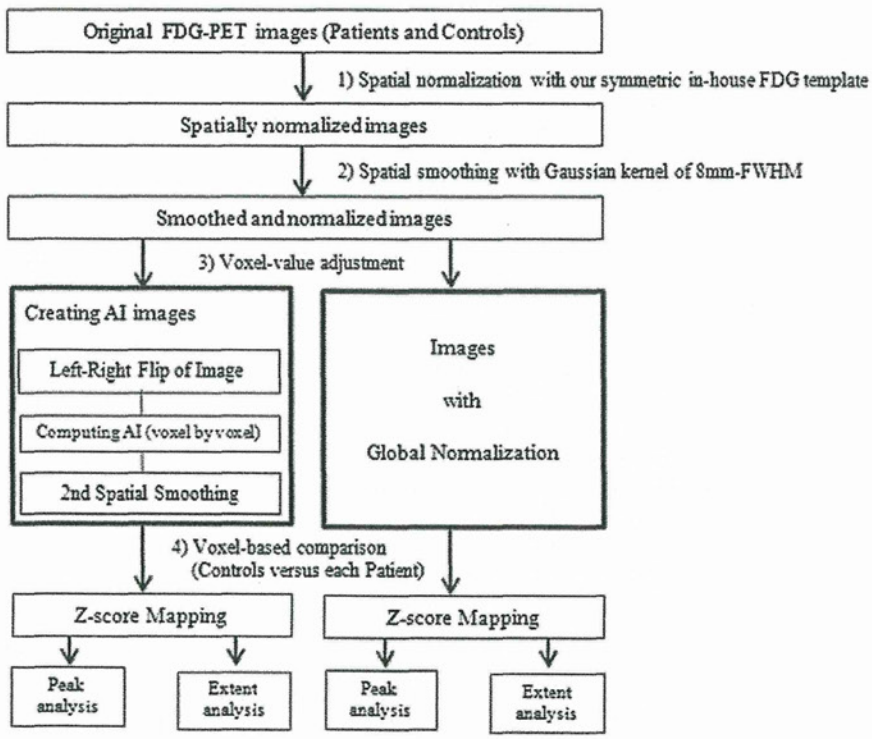

Fig. 1 The data analysis process: two types of voxel-value adjustments, the computing asymmetry index (AI) and global normalization, were performed after spatial normalization and smoothing. Then, a voxel-based comparison (*z*-score mapping) was performed for each type of voxel-value adjustment, followed by peak and extent analyses for each *z*-score map

made by reversing the mean image in the left–right direction. Third, by adding the flipped and non-flipped mean images, a symmetrical image was prepared as a semifinal template. Finally, a similar procedure was performed with the semifinal template, once again, that is, the original 20 control images were spatially normalized with the semifinal template, the 20 normalized images were averaged, a flipped image was made by reversing the mean image in the left–right direction, and the final symmetrical template was obtained by adding the flipped and non-flipped mean images.

All spatially normalized images were then smoothed using a three-dimensional isotropic Gaussian kernel with a full width at half maximum (FWHM) of 8 mm.

Voxel-value adjustment

Voxel values of normalized and smoothed images were adjusted by two methods. One method was to divide voxel values by the estimated average whole brain value of each normalized and smoothed image [16]. This method is the "global normalization with proportional scaling (GN)" generally used in SPM analysis for PET data. The other method was calculation of the AI. This method was as same as the procedure employed by Didelot and associates [11]. Each normalized and smoothed image was right and left reversed, and AI images were calculated with the non-flipped image and the corresponding flipped image using:

$$V_{AI} = (V_{nf} - V_f)/(V_{nf} + V_f) \quad (1)$$

where V_{AI} represents the AI image, V_{nf} is the non-flipped image, and V_f is the flipped image.

The second spatial smoothing was applied to each AI image using a three-dimensional isotropic Gaussian kernel with 4-mm FWHM.

Z-score mapping

Voxel-based comparisons between the patient and control groups were performed on voxel values adjusted with GN and with AI, as described above. The resulting images for the comparisons were mapped using z scores, calculated on a voxel-by-voxel basis using:

$$Z = (V_m - V_p)/SD, \quad (2)$$

where Z represents the z score, V_m the mean of the controls' corresponding voxel values, V_p the value of the patient's corresponding voxel, and SD the standard deviation of the controls' corresponding voxel values.

VOI of parahippocampal gyrus

To decide right- and left-VOIs for the bilateral hippocampal areas, we set the parahippocampal gyrus, based on the Talairach and Tournoux atlas, at the gyrus level using Talairach Deamon [17, 18]. The area of the parahippocampal gyrus was converted into the MNI space [19] and the symmetrical VOIs were defined as the overlapping areas of the right and left sides (the left-side area was flipped over to the right and vice versa) of the parahippocampal gyrus (Fig. 2).

Peak analysis

Peak analysis was performed for each z-score map of two types, one being the map with GN and the other the map with AI. The abnormal side was judged by the maximum z score, which had to exceed 2, in the VOIs of the parahippocampal gyrus bilaterally.

Extent analysis

Extent analysis was also performed for each z-score map of both types, one being the map obtained with GN and the other that obtained with AI. Abnormalities were judged based on extent, that is, the ratio of the number of voxels which had z scores exceeding a z-score threshold to the total number of voxels in the VOI. The extent was computed by varying the z-score threshold by 0, 0.5, 1, 1.5 and 2. Subsequently, the

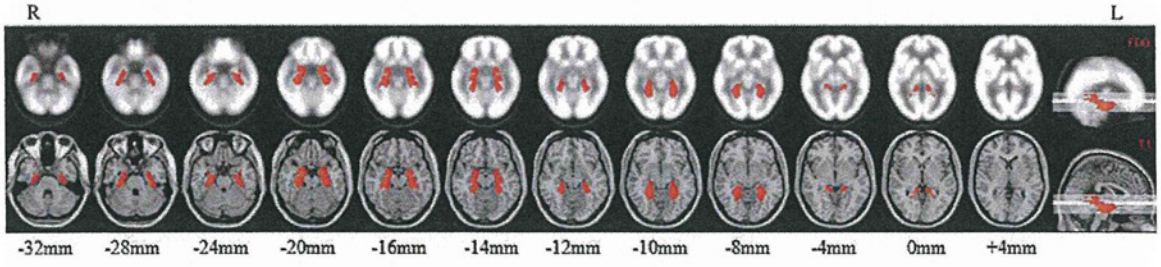

Fig. 2 A set of right and left volumes-of-interest (VOIs) in the parahippocampal gyrus was selected for determination of the side with the epileptogenic zone in a patient with mesial temporal lobe epilepsy. Transaxial and sagittal sections on the *upper row* indicate VOIs (*red regions*) on our in-house FDG template. The *lower images* indicate VOIs (*red region*) on a spatially normalized T_1-weighted magnetic resonance image. *Horizontal lines* on the sagittal sections correspond to transaxial slices displayed on the *left*. Numerical scales below the lower images show z coordinates on the Montreal Neurological Institute (MNI) space

side of the VOI exceeding the extent threshold was judged to be the abnormal side. In short, extent analysis was performed using two types of threshold: z score and extent. In this study, the abilities to accurately judge and determine optimum thresholds for z score and extent were evaluated as described in the following section.

Sensitivity, specificity and ROC analysis

The sensitivity and specificity of extent analysis were defined as follows. Sensitivity was the proportion of the number of patients in whom the side with the EZ was accurately judged as the abnormal side. Specificity was the proportion of patients in whom the non-abnormality was accurately judged on the side contralateral to the EZ. These sensitivity and specificity values were calculated by varying the extent threshold and used in the receiver operating characteristic (ROC) analysis. The ROC analysis was performed using the ROCKIT 1.1β2 program developed by Metz et al. [20] (http://xray.bsd.uchicago.edu/krl). The program calculates the area under the ROC curves (A_z), the statistical significance of the difference between the two A_z, accuracy, sensitivity and specificity. Accuracy and optimal threshold of extent were determined based on the value at the point at which sensitivity is the same as specificity on the ROC curve. Then, applying the PlotROC program (http://xray.bsd.uchicago.edu/krl), we drew ROC curves with the interpolated values statistically calculated. The extent analysis with AI at a z-score threshold of 0 was excluded, because the extent of either right- or left-side VOI always exceeded 50% with this method.

Table 1 Results of peak analysis with z-score mapping

	Correct	Incorrect	Rate (%)
Global normalization	12	5	70.6
Asymmetry index	15	2	88.2

The number in the "Correct" or "Incorrect" column is the number of patients in which the side with the epileptogenic zone was or not correctly identified. "Rate" is the rate of correct identifications

Results

Peak analysis

The results of peak analysis are shown in Table 1. The rate of correct answers was better with the AI method than with the conventional GN method. For 12 patients in whom the side harboring the EZ was correctly identified using both the AI and the conventional method, the peak z scores were 6.2 ± 1.6 (mean $\pm$ standard deviation) and 3.6 ± 1.0, respectively, and the difference in peak z scores between the AI and conventional methods was significant by paired Student's t test at $p < 0.001$ (two-tailed p value).

Extent analysis

The results of ROC analysis are shown in Table 2 and Fig. 3. Among all methods, the highest A_z of 0.971 was obtained at z-score thresholds of both 0.5 and 1 with the AI method. Applying the AI method at a z-score threshold of 0.5, the accuracy and the optimal extent threshold for judgment were 92 and 32.9%, respectively. With this extent threshold, the side harboring the EZ was correctly identified in 16 of 17 patients (94.1%). The extents at the ipsilateral and contralateral sides of the EZ were $70.3 \pm 22.3\%$ (mean $\pm$ standard deviation) and $11.3 \pm 13.2\%$, respectively, such that the difference in extent between the sides ipsilateral and contralateral to the EZ was significant by paired Student's t test at $p < 0.001$ (two-tailed p value). Applying the AI method at a z-score threshold of 1, the result of ROC analysis were also similar.

Among conventional GN methods, the highest A_z of 0.869 was obtained at a z-score threshold of 0.5, and the accuracy and the optimal extent threshold for judgment

Table 2 Receiver operating characteristic (ROC) curve results for the extent analysis

Asymmetry index						Global normalization				
Z	Extent-true (%)	Extent-false (%)	A_z	Ac (%)	Th (%)	Extent-true (%)	Extent-false (%)	A_z	Ac (%)	Th (%)
0	–	–	–	–	–	74.3 ± 22.6	33.2 ± 24.3	0.854	78	62.1
0.5	70.3 ± 22.3	11.3 ± 13.2	0.971	92	32.9	61.5 ± 23.7	19.9 ± 20.1	0.869	79	49.2
1	58.0 ± 24.7	5.7 ± 7.8	0.971	92	19.0	44.6 ± 23.4	10.6 ± 16.6	0.853	77	16.2
1.5	45.3 ± 25.4	2.5 ± 3.9	0.963	91	9.9	29.7 ± 20.7	5.7 ± 13.7	0.814	74	7.2
2	34.0 ± 23.4	1.0 ± 1.8	0.931	88	3.2	17.8 ± 15.5	3.1 ± 10.1	0.776	71	3.7

Values in "Extent-true" and "Extent-false" columns are presented as the mean $\pm$ standard deviation. "Ac" and "Th" indicate the accuracy and threshold, respectively, for the extent analysis at the point at which sensitivity is the same as specificity on the ROC curve

Z z-score threshold, *Extent-true* extent on the side harboring the epileptogenic zone in a patient with MTLE, *Extent-false* extent on the contralateral side, A_z area under the ROC curve

were 79 and 49.2%, respectively. With this extent threshold, the side harboring the EZ was correctly identified in 14 of 17 patients (82.4%). No significant difference in A_z between the AI method at a z-score threshold of 0.5 and the conventional method at a z-score threshold of 0.5 was detected by the z-score test ($p = 0.1017$, two-tailed p value). Similarly, there was no significant difference in A_z between the AI method at a z-score threshold of 1 and the conventional method at a z-score threshold of 0.5, as demonstrated by the z-score test ($p = 0.1017$, two-tailed p value).

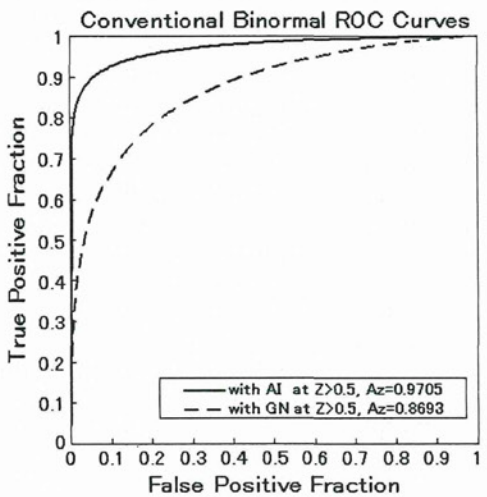

Fig. 3 Receiver operating characteristic (ROC) curves for the two methods employing the Asymmetry index (AI) and global normalization (GN) at the z-score threshold of 0.5

Representative z-score maps obtained by the AI and conventional GN methods are shown in Fig. 4.

Discussion

We applied AI, z-score mapping, and extent analysis techniques to preoperative FDG-PET in MTLE patients who were candidates for epilepsy surgery, and detected regional glucose hypometabolism. Moreover, we evaluated the detection utility of these methods to identify abnormalities in the unilateral hippocampal area later confirmed to harbor the EZ by surgical treatment and subsequent good seizure control. The AI method was more sensitive for detecting regional glucose hypometabolism and more accurate for identifying the EZ side than the conventional GN method. Automated identification of the side harboring the EZ showed improved accuracy with the combination of statistical z-score mapping employing AI and extent analysis based on VOIs of the parahippocampal gyrus.

Usefulness of SPM with AI

Similar to the results of previous studies on MTLE [10, 11], the AI technique was found to be more sensitive than the conventional GN technique for detecting regional glucose hypometabolism on unilateral PET images from MTLE patients as compared to those of a control group by automated analysis with a z-score peak (Table 1) and with extent analysis (Table 2; Fig. 3), although A_z values did not differ significantly between the AI and conventional methods.

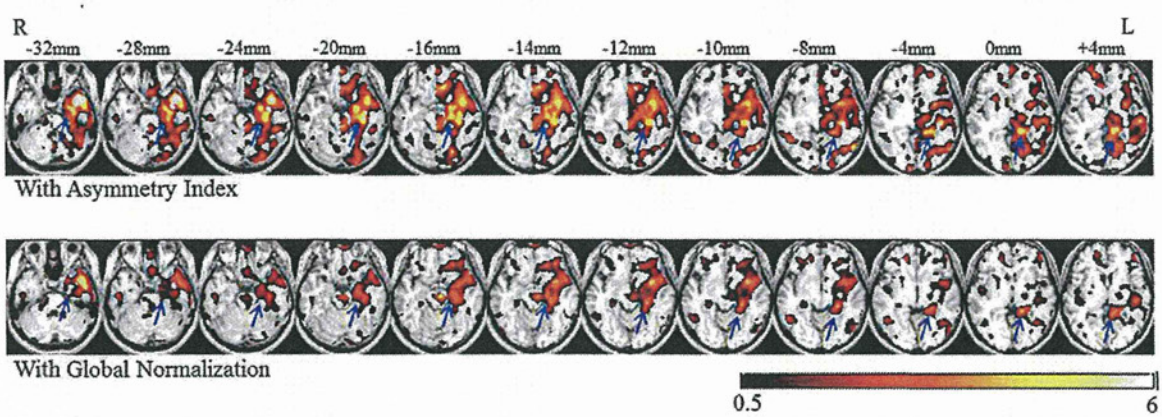

Fig. 4 Representative z-score maps obtained with the asymmetry index (AI *upper row*) and conventional global normalization (GN *lower row*) for comparison of FDG images from a patient with mesial temporal lobe epilepsy and controls. *Color-scaled* z-score maps are displayed as regions exceeding a z-score threshold of 0.5 on a spatially normalized T_1-weighted magnetic resonance image. *Numerical scales above the upper images* show z coordinates on the Montreal Neurological Institute (MNI) space. This patient's epileptogenic zone is to the *left* of the parahippocampal gyrus. Peak z scores with AI and GN are 6.0 (*left side*) and 3.7 (*left side*), respectively, by peak analysis. Extents (*left side*) with AI and GN for this patient are 90.8 and 78.0%, respectively. Z-score mapping with the AI shows glucose hypometabolism in the parahippocampal gyrus (*arrow*) to be more severe and widespread than that mapped with GN

Laterality on FDG-PET images is a very important piece of information for radiologists making a clinical diagnosis. Conventional voxel-based analyses, such as SPM, the easy *z*-score imaging system (eZIS) [21] and three-dimensional stereotactic surface projections (3D-SSP) [22], detect differences in voxel values (employing voxel-value adjustment, as with GN, normalization of the cerebellum count, and normalization pertaining to other reference areas) between control and patient groups at the same coordinates. Thus, abnormalities cannot be detected, if the patient's voxel value is within the deviation of the control group's voxel values, even if abnormal laterality is seen in the patient's image. On the other hand, the method employing inter-hemispheric AI used in the present study can detect abnormal laterality in a patient if the AI of the patient's voxel value exceeds that of the control group's deviation in the AI of the corresponding voxel, even if the patient's voxel value is within the deviation of the control group's voxel values.

Usefulness of extent analysis

As noted in "Introduction", regional glucose hypometabolism is often observed as an extensive area associated with EZ rather than as a small area associated with an epileptic focus. Hence, we studied two indicators (peak and extent) for automated determination of the side harboring the EZ employing FDG-PET in patients with unilateral MTLE. In the present study, the highest accuracy was obtained employing the method combining AI and extent analysis (*z*-score threshold = 0.5, extent threshold = 32.9%, accuracy = 92% and the side harboring the EZ was correctly identified in 16 of 17 patients). Moreover, with both the AI and the GN method, the extent analysis yielded a higher rate of correct EZ-side identification than the peak analysis. It is conceivable that these improvement of accuracy depended on two benefits of the extent analysis. First of the benefits is robustness for statistical noise, because the number of target voxels in the extent analysis is more than that in the peak analysis. Second of the benefits is the approach for clinical background that an extensive area of glucose hypometabolism associated with EZ is observed. These results suggest that the extent analysis may provide important information for detecting the region of abnormal glucose hypometabolism. The usefulness of extent analysis for identifying this abnormal region as compared with the severity of the abnormality has been reported, although prior studies examined regional cerebral blood flow (rCBF) using SPECT in Alzheimer disease (AD). Mizumura et al. [23] stated that studying the extent of the region of abnormal rCBF causing functional disorders was more rational than assessing the severity of the rCBF abnormality reflecting local tissue degeneration. Matsuda et al. [24] studied automated discrimination between very early AD patients and controls using three indicators (referred to as extent, severity and ratio) and noted in their report that the contention of Mizumura et al. may be supported by the fact that the discrimination power of the extent analysis was slightly higher than that of severity. Our present results, like those of both of the aforementioned reports, also showed the usefulness of extent analysis.

Technical limitations

Several technical limitations warrant discussion. First, in the present study, the normal control group was not age-, sex- and handedness-matched with each patient. Yanase and associates studied age-related FDG uptake using magnetic resonance imaging-based correction of the partial volume effect (PVE) [25]. Kawachi [26] and associates investigated sex and age differences and also inter-hemispheric laterality in cerebral glucose metabolism with a voxel-based analysis employing SPM in healthy right-handed volunteers. According to our literature search, there are no previous studies on inter-hemispheric laterality of glucose metabolism relevant to handedness. Whether there are age-, sex- and/or handedness-related inter-hemispheric AI changes in regional glucose metabolism remains uncertain, though several studies have raised these possibilities. Hence, for statistical analysis using AI of FDG-PET images, it is unknown whether or not an age, sex and handedness-matched control group is necessary.

The following (second, third and fourth) limitations were also mentioned by Didelot et al. [11]. Second, artifacts within a limited volume of several tens of voxels were centered over the inter-hemispheric midline, allowing AI to be used to generate a *z*-score map by applying a second spatial smoothing procedure to AI images. Such midline artifacts might hamper the interpretation of glucose hypometabolism in the mesial temporal lobe. However, these artifacts did not have a major impact in this study. The second spatial smoothing is related to FWHM; hence, further investigation of the influence of smoothing is necessary.

Third, the influence of symmetrization of the physiologically asymmetrical brain is unknown. Deformation of the brain, resulting from the normalization step for the symmetric template, differs between the left and right hemispheres. Brain deformation may influence the yield of AI analysis as a function of MTLE lateralization.

Fourth, the method employing AI cannot provide direct information as to whether an abnormal AI primarily reflects glucose hypermetabolism on one side or glucose hypometabolism on the other. In the case of bilateral MTLE, although not studied herein, the AI method might not provide adequate information about a bilateral absence

of abnormalities versus a unilateral abnormality. This drawback is compensated for by the *z*-score mapping with conventional GN using a low *z*-score threshold (e.g. 0 or 1).

Conclusion

In the present study, statistical *z*-score mapping with AI was more sensitive for detecting regional glucose hypometabolism and more accurate for identifying the side harboring the EZ using inter-ictal FDG-PET in unilateral MTLE than *z*-score mapping with conventional GN, when applied to the two approaches of peak analysis and extent analysis. Moreover, automated identification of the side harboring the EZ in unilateral MTLE was more accurate using a combination of statistical *z*-score mapping with AI and extent analysis based on VOIs of the parahippocampal gyrus.

References

1. Wiebe S, Blume WT, Girvin JP, Eliasziw M. A randomized, controlled trial of surgery for temporal-lobe epilepsy. N Engl J Med. 2001;345:311–88.
2. McIntosh AM, Kalnins RM, Mitchell LA, Fabinyi GC, Briellmann RS, Berkovic SF. Temporal lobectomy: long-term seizure outcome, late recurrence and risks for seizure recurrence. Brain. 2004;127:2018–30.
3. Lee DS, Lee JS, Kang KW, Jang MJ, Lee SK, Chung JK, et al. Disparity of perfusion and glucose metabolism of epileptogenic zones in temporal lobe epilepsy demonstrated by SPM/SPAM analysis on 15O water PET, [18F]FDG-PET, and [99mTc]-HMPAO SPECT. Epilepsia. 2001;42:1515–22.
4. Kim MA, Heo K, Choo MK, Cho JH, Park SC, Lee JD, et al. Relationship between bilateral temporal hypometabolism and EEG findings for mesial temporal lobe epilepsy: analysis of 18F-FDG PET using SPM. Seizure. 2006;15:56–63.
5. Kumar A, Juhasz C, Asano E, Sood S, Muzik O, Chugani HT. Objective detection of epileptic foci by 18F-FDG PET in children undergoing epilepsy surgery. J Nucl Med. 2010;51:1901–7.
6. Wong CH, Bleasel A, Wen L, Eberl S, Byth K, Fulham M, et al. The topography and significance of extratemporal hypometabolism in refractory mesial temporal lobe epilepsy examined by FDG-PET. Epilepsia. 2010;51:1365–73.
7. Ohta Y, Nariai T, Ishii K, Ishiwata K, Mishina M, Senda M, et al. Voxel- and ROI-based statistical analyses of PET parameters for guidance in the surgical treatment of intractable mesial temporal lobe epilepsy. Ann Nucl Med. 2008;22:495–503.
8. Kim YK, Lee DS, Lee SK, Kim SK, Chung CK, Chang KH, et al. Differential features of metabolic abnormalities between medial and lateral temporal lobe epilepsy: quantitative analysis of (18)F-FDG PET using SPM. J Nucl Med. 2003;44:1006–12.
9. Lee JJ, Kang WJ, Lee DS, Lee JS, Hwang H, Kim KJ, et al. Diagnostic performance of 18F-FDG PET and ictal 99mTc-HMPAO SPET in pediatric temporal lobe epilepsy: quantitative analysis by statistical parametric mapping, statistical probabilistic anatomical map, and subtraction ictal SPET. Seizure. 2005;14:213–20.
10. Van Bogaert P, Massager N, Tugendhaft P, Wikler D, Damhaut P, Levivier M, et al. Statistical parametric mapping of regional glucose metabolism in mesial temporal lobe epilepsy. Neuroimage. 2000;12:129–38.
11. Didelot A, Mauguiere F, Redoute J, Bouvard S, Lothe A, Reilhac A, et al. Voxel-based analysis of asymmetry index maps increases the specificity of 18F-MPPF PET abnormalities for localizing the epileptogenic zone in temporal lobe epilepsies. J Nucl Med. 2010;51:1732–9.
12. Engel J Jr, Van Ness PC, Rasmussen TB, Ojemann LM. Outcome with respect to epileptic seizure. In: Engel Jr J, editor. Surgical treatment of the epilepsies. 2nd ed. New York: Raven Press; 1993. p. 609–21.
13. Collins DL, Neelin P, Peters TM, Evans AC. Automatic 3D intersubject registration of MR volumetric data in standardized Talairach space. J Comput Assist Tomogr. 1994;18:192–205.
14. Talairach J, Tournoux P. Co-planar stereotaxic atlas of the human brain. New York: Thieme; 1988.
15. Sakai Y, Kumano H, Nishikawa M, Sakano Y, Kaiya H, Imabayashi E, et al. Cerebral glucose metabolism associated with a fear network in panic disorder. Neuroreport. 2005;16:927–31.
16. Fox PT, Mintun MA, Reiman EM, Raichle ME. Enhanced detection of focal brain responses using intersubject averaging and change-distribution analysis of subtracted PET images. J Cereb Blood Flow Metab. 1988;8:642–53.
17. Lancaster JL, Rainey LH, Summerlin JL, Freitas CS, Fox PT, Evans AC, et al. Automated labeling of the human brain: a preliminary report on the development and evaluation of a forward-transform method. Hum Brain Mapp. 1997;5:238–42.
18. Lancaster JL, Woldorff MG, Parsons LM, Liotti M, Freitas CS, Rainey L, et al. Automated Talairach Atlas labels for functional brain mapping. Hum Brain Mapp. 2000;10:120–31.
19. Brett M, Johnsrude IS, Owen AM. The problem of functional localization in the human brain. Nat Rev Neurosci. 2002;3:243–9.
20. Metz CE, Herman BA, Roe CA. Statistical comparison of two ROC-curve estimates obtained from partially-paired datasets. Med Decis Mak. 1998;18:110–21.
21. Kanetaka H, Matsuda H, Asada T, Ohnishi T, Yamashita F, Imabayashi E, et al. Effects of partial volume correction on discrimination between very early Alzheimer's dementia and controls using brain perfusion SPECT. Eur J Nucl Med Mol Imaging. 2004;31:975–80.
22. Minoshima S, Frey KA, Koeppe RA, Foster NL, Kuhl DE. A diagnostic approach in Alzheimer's disease using three-dimensional stereotactic surface projections of fluorine-18-FDG PET. J Nucl Med. 1995;36:1238–48.
23. Mizumura S, Kumita S, Cho K, Ishihara M, Nakajo H, Toba M, et al. Development of quantitative analysis method for stereotactic brain image: assessment of reduced accumulation in extent and severity using anatomical segmentation. Ann Nucl Med. 2003;17:289–95.
24. Matsuda H, Mizumura S, Nagao T, Ota T, Iizuka T, Nemoto K, et al. Automated discrimination between very early Alzheimer disease and controls using an easy Z-score imaging system for multicenter brain perfusion single-photon emission tomography. Am J Neuroradiol. 2007;28:731–6.
25. Yanase D, Matsunari I, Yajima K, Chen W, Fujikawa A, Nishimura S, et al. Brain FDG PET study of normal aging in Japanese: effect of atrophy correction. Eur J Nucl Med Mol Imaging. 2005;32:794–805.
26. Kawachi T, Ishii K, Sakamoto S, Matsui M, Mori T, Sasaki M. Gender differences in cerebral glucose metabolism: a PET study. J Neurol Sci. 2002;199:79–83.

Neurol Sci (2012) 33:1355–1364
DOI 10.1007/s10072-012-0949-5

ORIGINAL ARTICLE

State-dependent precursors of seizures in correlation-based functional networks of electrocorticograms of patients with temporal lobe epilepsy

Hirokazu Takahashi · Shuhei Takahashi · Ryohei Kanzaki · Kensuke Kawai

Received: 1 October 2011 / Accepted: 10 January 2012 / Published online: 21 January 2012

Abstract Accurate prediction of epileptic seizures will open novel therapeutic possibilities for patients with intractable epilepsy. We attempted to identify precursors of seizures in the functional networks of electrocorticograms by applying graph theory. Long-term electrocorticograms for periods of 39–76 h from three patients with temporal lobe epilepsy were investigated using pair-wise cross-correlations. Time-varying network properties suggested that there were several distinct brain states. Although functional networks during seizures could be characterized as having a regular topography, no consistent characteristics of functional networks were found immediately prior to seizure onsets. However, it was found that seizures under an identical state were followed by similar transients of the network properties. These results suggest that network properties themselves could not serve as reliable predictors of seizure onset. Yet, some significant pre-seizure changes in the parameters tested appear likely to depend on the brain state. To predict seizures, it may be necessary to take into consideration the states of the brain. In addition to stationary network properties we characterized in the present study, dynamic interactions of epileptic activities with the network might be taken into account to predict the spread of a seizure.

Keywords Graph theory · Electrocorticogram · Epilepsy · Seizure prediction · Seizure detection

H. Takahashi · R. Kanzaki
Research Center for Advanced Science and Technology, The University of Tokyo, Komaba 4-6-1, Meguro-ku, Tokyo 153-8904, Japan

H. Takahashi · S. Takahashi · R. Kanzaki
Graduate School of Information Science and Technology, The University of Tokyo, Hongo 7-3-1, Bunkyo-ku, Tokyo 113-8656, Japan

H. Takahashi
PRESTO, JST, 4-1-8 Honcho Kawaguchi, Saitama 332-0012, Japan

K. Kawai (✉)
Department of Neurosurgery, Graduate School of Medicine, The University of Tokyo, Hongo 7-3-1, Bunkyo-ku, Tokyo 113-8655, Japan
e-mail: kenkawai-tky@umin.net

Introduction

Accurate prediction of epileptic seizures will bring considerable benefits for a significant population of patients with drug-resistant and intractable epilepsy. For example, warnings of oncoming seizure would reduce the grave threats posed by sudden, unforeseen seizures. Furthermore, on-demand interventions such as direct electrical stimulation or biofeedback could be established as novel therapeutic options to prevent seizures [1–4].

Seizure prediction based on scalp electroencephalogram (EEG) results has long been attempted since the 1970s [5], in which correlations to systematic preictal changes in linear [6–8] and non-linear parameters [9–11] have been explored. Despite these extensive efforts, prediction accuracy has thus far never been sufficiently reliable for practical use.

Recently, an increasing number of studies have investigated prediction based on intra-cranial EEG, or electrocorticogram (ECoG) results, which provide a significantly better signal-to-noise ratio and spatial resolution than scalp EEGs. Some of these studies suggest that potential seizure precursors are widely distributed in areas remote from the

Table 1 Subjects

	Age at surgery	Gender	Location of epileptic focus	Type of seizure	Outcome of surgery (Engel class)	# of seizure during recording	Total recording time (hours)
Pt #1	40	M	Left mediobasal temporal lobe	SP, CP, SG	Id	2	39
Pt #2	47	M	Right lateral temporal lobe	SP, CP, SG	Ia	2	67
Pt #3	36	F	Left temporal tip/uncus	SP, CP	Ia	5	76

SP simple partial, *CP* complex partial, *SG* secondarily generalized

Table 2 Locations of implanted electrodes

Subject	Electrode #	Hemisphere	Location
Pt #1	#1–#4	Left (*LH*)	Uncus (*un*)
	#5–#12		Mediobasal temporal lobe (*mb*)
	#13–#16		Posterobasal temporal lobe (*pb*)
	#17–#22		Orbitofrontal surface (*os*)
	#23–#70		Lateral temporal lobe (*lt*)
	#71–#78	Right (*RH*)	Mediobasal temporal lobe
	#79–#86		Lateral temporal lobe
Pt #2	#1–#4	Left	Uncus
	#5–#12		Mediobasal temporal lobe
	#13–#16		Posterobasal temporal lobe
	#17–#22		Broca's area (*Br*)
	#23–#70		Lateral temporal lobe
	#71–#74	Right	Uncus
	#75–#82		Mediobasal temporal lobe
	#83–#86		Posterobasal temporal lobe
	#87–#92		Broca's area
	#93–#120		Lateral temporal lobe
Pt #3	#1–#4	Left	Temporal tip (*tt*)
	#5–#8		Uncus
	#9–#16		Mediobasal temporal lobe
	#17–#24		Posterobasal temporal lobe
	#25–#30		Hippocampus (*hc*)
	#31–#74		Lateral temporal lobe
	#75–#82		Uncus
	#75–#82	Right	Mediobasal temporal lobe
	#83–#90		Lateral temporal lobe

Abbreviations as used in Fig. 4

epileptic focus, occasionally in the contralateral hemisphere [12–16]. This suggests an emphasis be placed on functional network properties that allow seizures to spread. Therefore, multi-variate measures such as inter-electrode correlation and synchrony have come to be considered better predictors of seizure onset than conventional univariate measures [17–19]. These multi-variate measures can be summarized as global network properties using a graph theory approach. The global network properties can potentially serve as useful predictors [20, 21].

Furthermore, recent growth in storage capacity for data has made viable continuous multi-day recordings, which provide an opportunity to investigate confounding variables such as circadian fluctuation of bodily state and vigilance state [22–24]. These variables have long been considered to affect the ability to predict seizures [7], but have not yet been intensively investigated.

In the current study, with a goal of improving seizure prediction, we investigate long-term ECoG results of patients suffering from temporal lobe epilepsy. First of all, we characterize how the state of the brain varies hour by hour in terms of global properties of correlation-based functional networks. Secondly, we attempt to identify precursors of seizures in these functional networks. Thirdly, we test whether these precursors depend on the brain state.

Materials and methods

Subjects

Three patients (Patient #1–Patient #3) were randomly selected from a group that underwent surgical treatment for drug-resistant epilepsy (Table 1). The patients selected had seizures that involved the medial or lateral temporal lobe at onset and that had comparable seizure patterns. All patients had a comprehensive presurgical evaluation including a detailed history review and neurological examination, neuropsychological testing, scalp EEG with sphenoidal leads, magnetoencephalography, magnetic resonance imaging (MRI), fluoro-2-deoxy-D-glucose positron emission tomography, Technetium-99m ethyl cysteinate dimer single photon emission computed tomography (SPECT) (123)I-iomazenil SPECT, and long-term ECoG monitoring with multiple subdural electrodes. Abolishment of seizures was verified based on postsurgical observation for two or more years in all patients.

Long-term ECoG recordings

Electrocorticogram recording was performed during long-term video-ECoG monitoring in the University of Tokyo Hospital. It was carried out as a part of the patient's routine clinical care. Informed consent was obtained from all patients for implantation of intracranial electrodes, surgical treatment, and separately for research use of the ECoG data. Research use of ECoG data, including this study, was approved by the local ethical committee.

Following temporal craniotomy, grid electrodes were placed on the lateral frontotemporal cortices. For the mediobasal temporal region, a trapezoid grid with eight contacts aligned in a T-shape fashion was used in combination with strip electrodes. Using fluoroscopy to align the four medial contacts of the trapezoid grid at the same height as and just behind the tip of the dorsum sellae enabled the four contacts to cover the parahippocampal gyrus in the anteroposterior direction. Table 2 shows the locations of the implanted electrodes. Figure 1 shows the representative overlaying images of 3D reconstruction from the computed tomography (CT) and MRI of Patient #1.

The original reference electrode is a scalp reference Cz. Signals were simultaneously monitored at all of the active electrodes by a 128-channel EEG recording system (Nicolet) without any digital filtering and stored on a hard disk with an A/D resolution of 16 bits/sample and a sample rate of 400 Hertz (Hz).

The EEG signals were first visually analyzed by an experienced epileptologist/epilepsy surgeon (K.K), and typical seizures were selected. Video images of the patients around the time of the EEG seizures were inspected as well. Only seizures in which an EEG seizure preceded or started simultaneously with clinical signs of a seizure were included in this study.

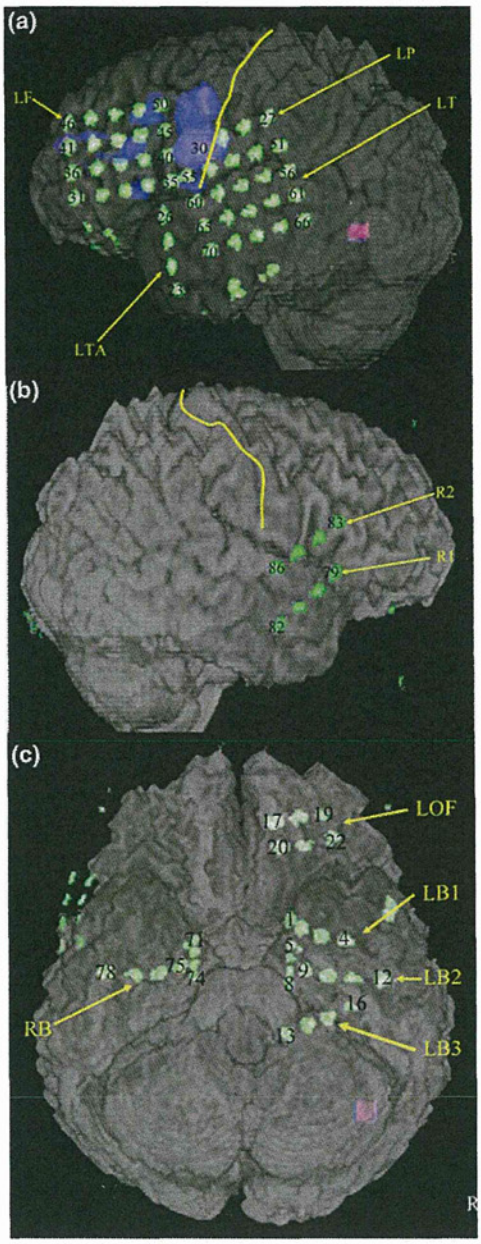

Fig. 1 Representative 3D reconstruction from computed tomography (CT) overlaying CT and MRI images of patient (Pt.) #1. **a** Left side. **b** Right side. **c** Base

Data analysis

For specific frequency bands, functional networks within n recording sites, or n nodes (n = 86–120), were estimated

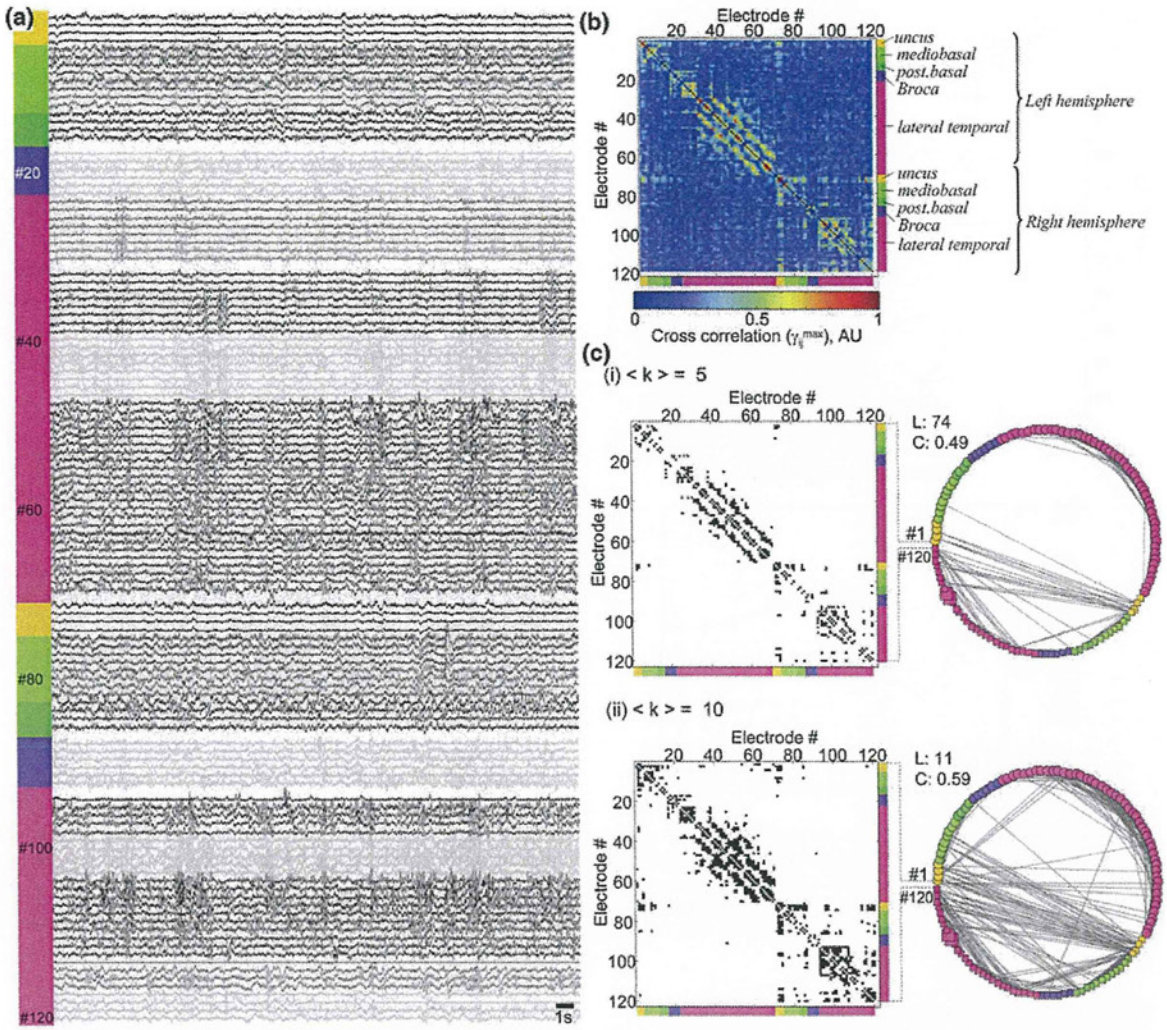

Fig. 2 Analytical procedure. **a** ECoG signals in a representative sliding window. The signals were aligned according to the identification number of the electrode (#1–#120). Regions of each electrode are designated by a *ticked band* at the *left* edge as defined in (**b**). Signals from an identical electrode array within a given area are drawn in the same gray level. **b** Matrix of normalized cross-correlation function, γ_{ij}^{max}. The location of each electrode is indicated in the *right* margin. **c** Adjacency matrices, a_{ij} (*left*), and graph structures of functional networks (*right*). The threshold, T, to binarize γ_{ij}^{max} was determined according to the average degree of graph: **i** $\langle k \rangle = 5$; and **ii** $\langle k \rangle = 10$. A filled element in the adjacency matrices indicates that a link exists between the corresponding nodes. Markers in the graphs correspond to recording sites (#1–#120), and the *ticked markers* indicate regions as defined in (**b**). *Circles* and *squares* in the graphs indicate nodes in the left and right hemispheres of the brain, respectively, and large markers indicate the locations of epileptic foci. On the upper *left* hand of the graph, the values of L and C are indicated

on the basis of a pair-wise measurement of maximum linear cross-correlation and characterized on the basis of graph theory [20, 21].

Electrocorticogram signals were first divided into five frequency bands by FFT filters: δ 1–3 Hz; θ 4–7 Hz; α 8–13 Hz; β 14–30 Hz; and γ 30–64 Hz. In each band, functional links between any pair of recording sites ($i, j \in [1, n]$) were defined in a given sliding window using the following normalized cross-correlation function:

$$\gamma_{ij}^{\max} = \max_{\tau} \left\{ \frac{c(x_i, x_j)(\tau)}{\sqrt{c(x_i, x_i)(0)\, c(x_j, x_j)(0)}} \right\}$$

where

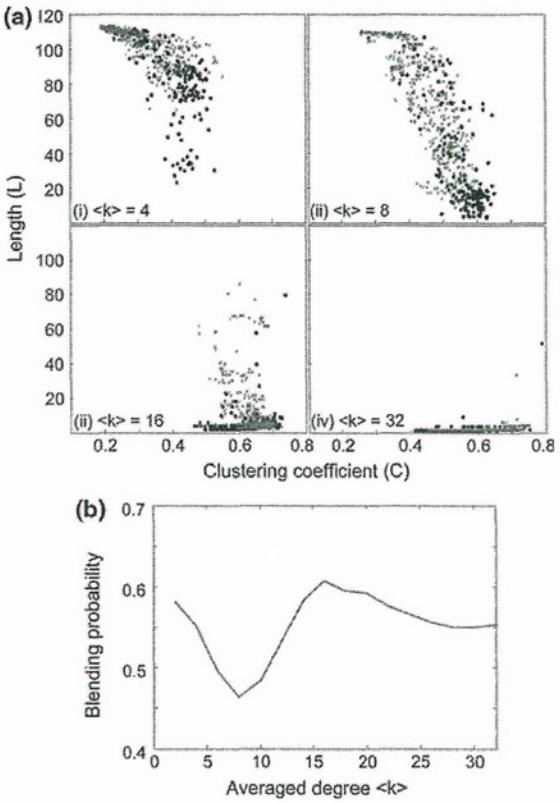

Fig. 3 Optimization of average degree. **a** Distribution of the average shortest path length, L, and the average cluster coefficient, C, at various values of $\langle k \rangle$. *Dark circles* and *light crosses* correspond to samples from pre-seizure states and interictal states, respectively. **b** Blending probability of pre-seizure state compared with interictal state as a function of $\langle k \rangle$

Table 3 $\langle k \rangle$ used as threshold in network characterization

	Delta	Theta	Alpha	Beta	Gamma
Pt #1	6	6	6	10	8
Pt #2	12	10	8	8	6
Pt #3	14	10	6	8	10

$$c(x_i, x_j)(\tau) = \begin{cases} \sum_{t=1}^{w-\tau} x_i(t+\tau)\, x_j(t), & \tau \geq 0 \\ c(x_j, x_i)(-\tau), & \tau < 0 \end{cases}$$

denotes the linear cross-correlation function quantifying the similarity of two signals x_i and x_j with a time lag of τ. $\gamma_{ij}^{\max}$ is confined to [0, 1] with high values indicating the two signals have a similar course over time though there is a possible time lag. The duration of the sliding window, w, was relatively long, 25 s in the current study, in order to characterize temporally stable links. The duration of the step of sliding was in increments of 60 s for the entire long-term data sets, and 1 s for data for the time period within 20 min before or after the clinical onset of seizures.

$\gamma_{ij}^{\max}$ was then binarized according to an arbitrary threshold, T, and the adjacency matrix, a_{ij}, was derived:

$$a_{ij} = \begin{cases} 1, & i \neq j \wedge \gamma_{ij}^{\max} \geq T \\ 0 & \text{otherwise.} \end{cases}$$

Based on a_{ij}, the properties of this functional network, or graph, were characterized in terms of degree distribution, average shortest path length, and cluster coefficient. The degree at each node was defined as:

$$k_i = \sum_{j=1}^{n} a_{ij}.$$

The average shortest path length was defined as:

$$L = \frac{2}{n(n-1)} \sum_{i>j} d_{ij}$$

where d_{ij} is the smallest number of links that can connect nodes i and j. When there was no path between two nodes, $d_{ij} = n$ was adopted. As a measure of the typical separation between two nodes in the graph, L is thus confined to $[1, n]$.

The cluster coefficient at node i was defined as:

$$C_i = \frac{2}{k_i(k_i-1)} E_i$$

where k_i denotes the number of nodes with a direct link from node i, and thus k_i $(k_i-1)/2$ means the number of allowable links within these k_i neighboring nodes, and E_i denotes the total number of links that actually exist in the neighboring nodes. The cluster coefficient of the network was then determined as.

$$C = \frac{1}{n} \sum_{i=1}^{n} E_i$$

C is confined to [0, 1], evaluating the cliquishness of a typical neighborhood.

Because L and C depended on T, T was optimized such that distributions of L and C in pre-seizure periods became most distinct from those in interictal periods. Sample distributions in L–C plane were first estimated for the pre-seizure group and interictal group. The pre-seizure group included samples from 10-min period before the first onset of clinical seizures with a time step of 1 s, and the interictal group was sampled from the whole dataset with a time step of 20 min. This distribution of L and C from either pre-seizure group or interictal group was used to estimate a probability of the corresponding group membership for each sample, assuming that the squared Mahalanobis' generalized distance in L–C plane is distributed as Chi-squared with 2 degree of freedom. For all of pre-seizure samples, the probability of interictal group membership

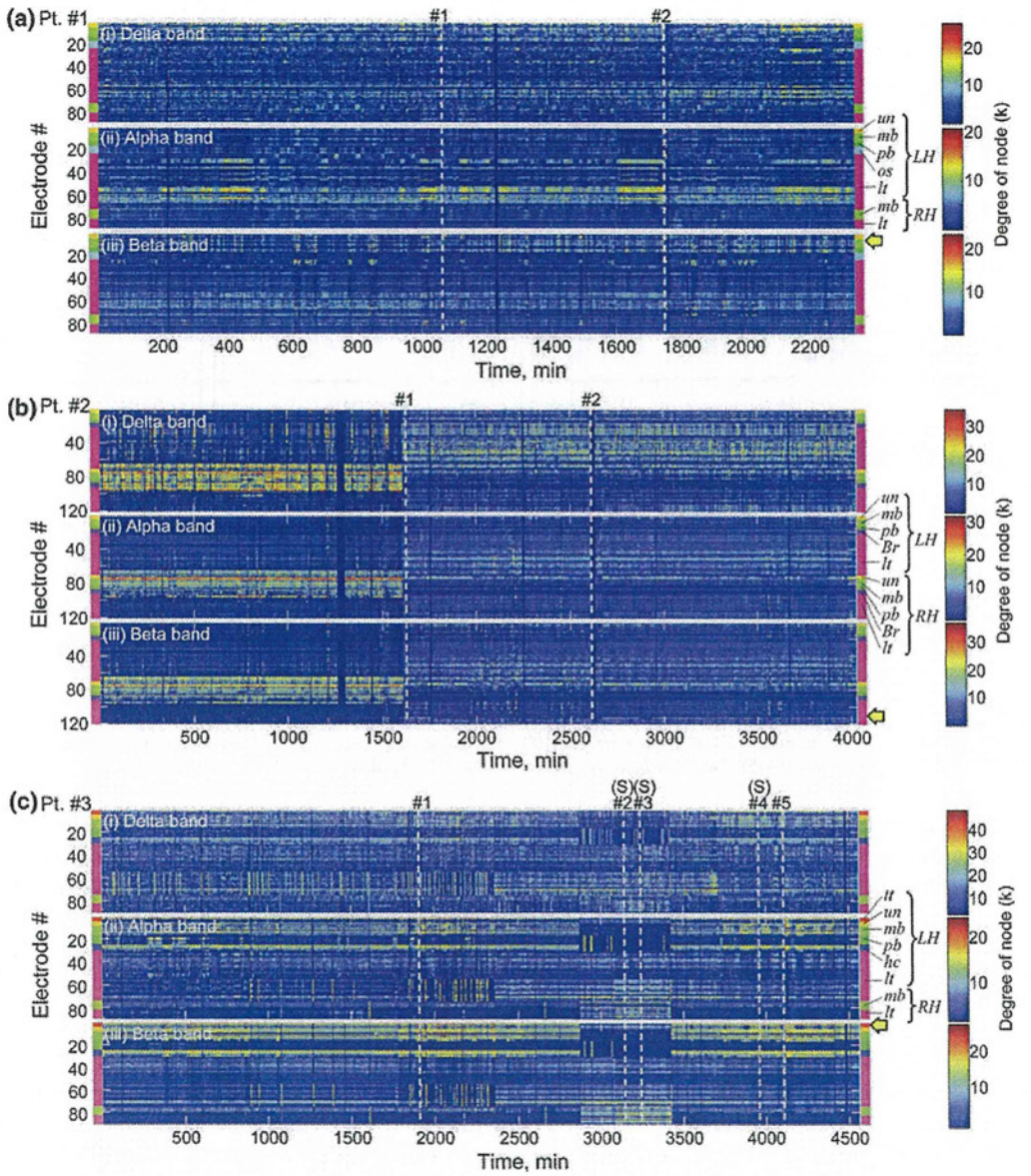

Fig. 4 Long-term characterization of degree distribution for each subject: **a** Pt. #1, **b** Pt. #2, **c** Pt. #3. The degree distributions shown are obtained at the indicated time and electrode for the indicated frequency bands: **i** delta, **ii** alpha, **iii** beta. Abbreviated locations of each electrode are indicated on the *right* and are defined in Table 2. A *broken line* indicates the occurrence of a seizure. Some seizures were simple partial seizures (labeled S), while others were complex partial seizures

was averaged to evaluate how often samples from the pre-seizure period belonged to interictal periods, and this average probability was defined as a blending probability. The blending probability was obtained as a function of the average degree. Because a low blending probability suggests that the properties of graphs, i.e., L and C, during the pre-seizure period are distinct from those during interictal periods, T was determined such that the graph has the optimal average degree, where the lowest blending probability was achieved.

Results

Figure 2a shows ECoG signals in a representative sliding window, from which the alpha-band cross-correlation

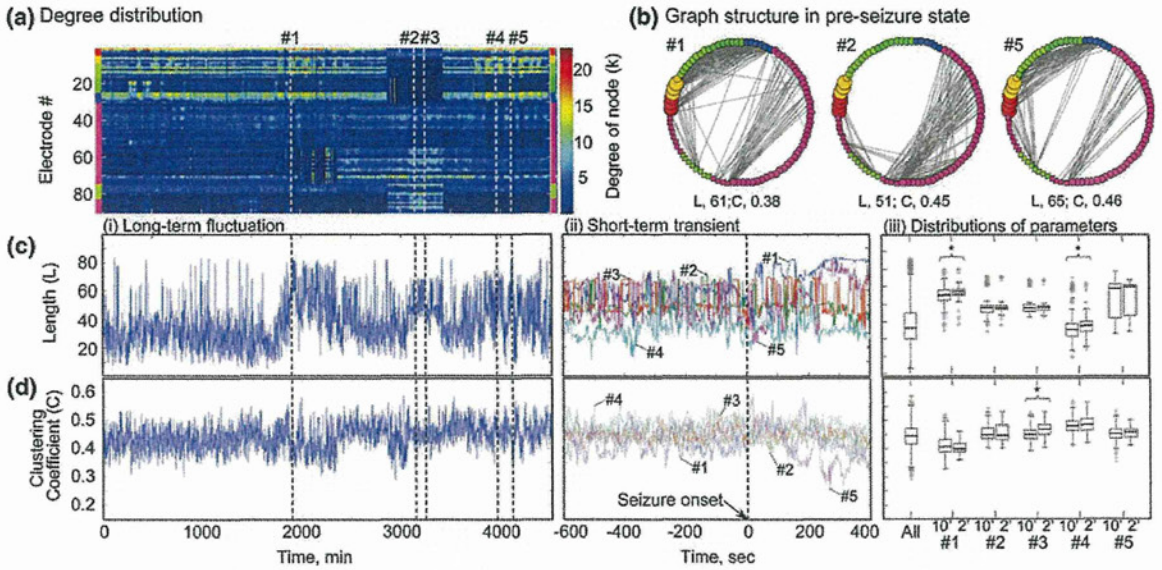

Fig. 5 Representative analyses in the alpha band for Pt. #3. **a** Degree distribution. **b** Graph structures at 10 min prior to onset of seizures #1, #2 and #3. The values of *L* and *C* are indicated at the *bottom* of each graph. **c** Average shortest path length (*L*): **i** Long-term characterization, **ii** Short-term transient characterization around the time of the onset of seizures, **iii** Distribution for the entire period, and for pre-seizure periods of two minutes (2′) and ten minutes (10′) before the onset of each seizure (#1–#5). On each *box*, the central mark is the median, and the edges of the *box* are the 25 and 75th percentiles. The whiskers extend to the most extreme data points not considered outliers. Data points that are larger than the 75th percentile or smaller than the 25th percentile by 1.5 times the inter-quartile range were considered to be outliers. The outliers were plotted individually using a '+' mark. An *asterisk* indicates statistical significance between a given pair (Mann–Whitney's *U* test; $^*p < 0.01$). **d** Average cluster coefficient (*C*)

matrix, $\gamma_{ij}^{\max}$, was obtained as shown in Fig. 2b. Most of the high correlations were found around the diagonal, indicating that nearby sites in the same anatomically defined region tended to be tightly linked, yet some pairs between inter-areal or inter-hemispherical sites also showed relatively high correlations. In order to characterize the properties of $\gamma_{ij}^{\max}$ as a graph, two representative adjacent matrices, a_{ij}, were obtained in Figs. 2c i, ii, in which the thresholds were determined such that the average degrees of nodes $\langle k_i \rangle$ became five and ten, respectively, demonstrating how a_{ij}, and thereby, the properties (*L* and *C*), as well as the structure of graphs, depended on the threshold.

At different thresholds, Fig. 3a shows how *L* and *C* were distributed over a long time scale during interictal periods and also in a confined pre-seizure period of 10 min before the first onset of clinical seizures. From these plots, the blending probabilities were derived as a function of average degree as shown in Fig. 3b. The optimal average degree was then determined, where the blending probability was minimized. Table 3 shows thus-obtained average degrees, which are used below to characterize a functional network in each frequency band for each patient.

For each patient Fig. 4 shows how a degree of node was distributed among recording sites in the band-specific functional networks and how the distributions of degree changed with time. For example, in patient #1, high-degree recording sites were often found in the alpha band within a confined region in the left lateral temporal lobe, thus potentially serving as a hub in this network (Fig. 4a, ii), while epileptic foci in the left mediobasal temporal lobe had relatively high degrees in the delta and beta bands (Fig. 4a, i, iii). In addition, in patients #2 and #3, the patterns of degree distribution, k_i, suggest that there are several distinct brain states. In patient #2, high-degree recording sites moved from the right hemisphere to the left hemisphere during the recording (Fig. 4b). Both of the seizures in patient #2 occurred in the latter state with high-degree sites in the left hemisphere. In patient #3, the brain states were likely to vary from hour to hour, and seizures did not always occur under a specific state; i.e., degree distribution patterns for seizures #1, #4 and #5 appeared to be distinct from those for seizures #2 and #3 (Fig. 4c). These states are long-lasting on the order of a day (e.g., in Pt. #2, >2400 min after seizure #1; in Pt. #3, >2700 min from the beginning of recording) and thus may not be attributed to shorter changes of state such as sleep cycle, wake/sleep cycle, or vigilance states.

In Fig. 5, representative analyses in the alpha band of patient #3 show how the structure and properties of functional networks depend on the states defined by the degree

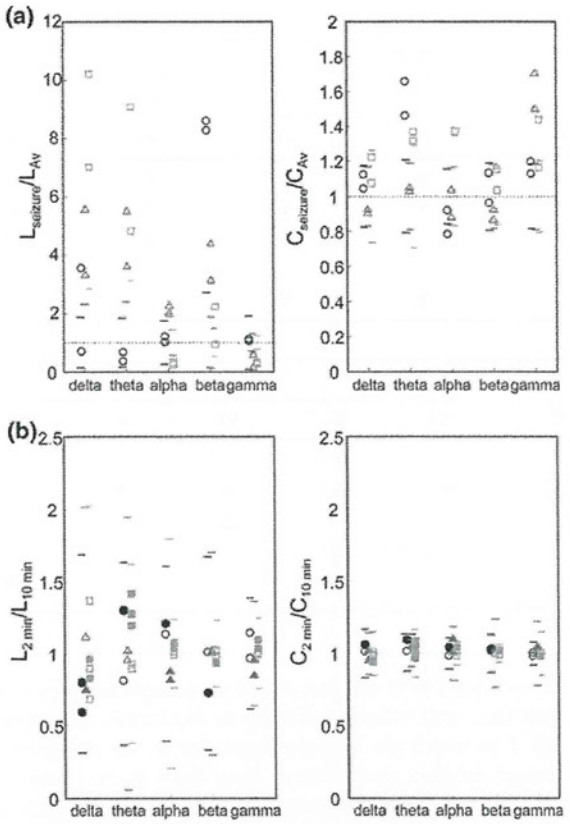

Fig. 6 Band-specific characterization of L and C. **a** Values of L and C during complex partial seizures ($L_{seizure}$ and $C_{seizure}$) were compared to those averaged over the long-term (L_{Av} and C_{Av}). Standard deviations of $L_{seizure}/L_{Av}$ and $C_{seizure}/C_{Av}$ are indicated by *small lines* for each patient in each band. **b** Values of L and C 2 min before seizures (L_{2min} and C_{2min}) were compared to those 10 min (L_{10min} and C_{10min}) before seizures. Symbols indicate subjects as follows: *circle* Pt. #1, *triangle* Pt. #2, *square* Pt. #3. *Filled symbols* indicate significant changes (see Table 4)

distribution in Fig. 5a. As shown in Fig. 5b, the structure of the functional network at 10 min prior to seizure #2 was distinct from those prior to seizures #1 and #5, confirming a close link between network structure and brain state. Figure 5c, i; d, i show the variation of L and C with time over a long timeframe. The results suggest that global trends may be associated with a change of brain states. The transient traces of L and C around the time of the onset of each seizure are plotted in Fig. 5c, ii; d, ii, respectively, in order to examine whether these properties serve as a predictor of seizures. From these data, boxplots in Fig. 5c, iii; d, iii show the distributions of L and C, respectively, for the timeframes indicated. In some parameters, distribution 10 min (10′) and 2 min (2′) before seizure onset were significantly different (Mann–Whitney's U test, $p < 0.01$). Specifically, increases in L were seen just before impending seizures #1 and #4 and increases in C preceded seizure #3. These parameters may be predictive signs of seizures.

In Fig. 6a, L and C during complex partial seizures ($L_{seizure}$ and $C_{seizure}$) were compared to L and C averaged over the long term (L_{Av} and C_{Av}). Aberrant values during seizures were often observed to be large L and C values, corroborating previous reports that functional networks during seizures are characterized as having a consistent, rather than random, topology [20, 21].

Similarly, in Fig. 6b, the averages of L and C 2 min before the onset of seizures (i.e., L_{2min} and C_{2min}) were compared with those 10 min before the onset of seizures (i.e., L_{10min} and C_{10min}). In comparison to apparent alterations of network properties during seizures (Fig. 6a), the differences in L and C 10 min and 2 min before the onset of seizures were less clear, yet there were significant differences in some parameters when L_{2min} and C_{2min} were compared to L_{10min} and C_{10min}, respectively (Mann–Whitney's U test, $p < 0.01$). For all seizures observed, Table 4 summarizes band-specific significant changes of L_{2min} and C_{2min} compared to L_{10min} and C_{10min}, respectively. These results indicate that in some cases L and C decrease rather than increase prior to the onset of seizures, suggesting that, unlike during seizures, pre-seizure states cannot be characterized as a shift toward regular networks. The directions of significant changes in L and C were sometimes different among seizures within an identical subject, yet were likely identical under similar states as defined by degree distribution (Fig. 4). Verification of this hypothesis entails testing 60 possible pairs of parameters since there are ten parameters (i.e., L and C each for 5 frequency bands) and 6 possible pairs of seizures with the same state (i.e., 1 for patient. #1, 1 for patient #2, and 4 for patient #3 [seizure sets #1 and #4, #1 and #5, #4 and #5, and #2 and #3]). Among these 60 possible pairs with the same state, nine pairs showed identical changes (5 Ls and 4 Cs) while only one pair showed an opposite change (C in delta band of patient #2), suggesting that, within identical states, consistent changes of the network parameters immediately preceding the onset of a seizure, if any, are not a coincidence (i.e., 9/60 vs. 1/60; z test, $p = 0.00104$).

Discussion

In the current study, we have characterized long-term ECoG signals on the basis of pair-wise cross-correlations, and attempted to identify precursors of seizures in terms of functional network properties (Fig. 2). First, time-varying network properties suggested that there were several distinct brain states. Because these states lasted for more than

Table 4 Significant pre-seizure changes of band-specific L and C found in each patient

	Pt #1				Pt #2			
	L		C		L		C	
	#1	#2	#1	#2	#1	#2	#1	#2
Delta	▼	▼		△	▼		△	▼
Theta	△			△	▼	▼	△	△
Alpha	△		△				△	△
Beta		▼	△					
Gamma					▼	▼		△

	Pt #3									
	L					C				
	#1	#2	#3	#4	#5	#1	#2	#3	#4	#5
Delta		▼	▼				▼			
Theta			△	△	△	▼	△	△	▼	
Alpha	△			△				△		
Beta		▼					△			△
Gamma			△		△					▼

△ increase, ▼ decrease (Mann–Whitney's U test, $p < 0.01$)

a day (e.g., in Pt. #2, >2400 min after seizure #1; in Pt. #3, >2700 min from the beginning of recording), they were likely unrelated to sleep cycle, wake/sleep cycle or vigilance state (Fig. 4). Second, while functional networks during seizure were possible to characterize as having a consistent topography, no consistent characteristics of functional networks were found immediately prior to the onset of seizures, indicating that network properties themselves could not serve as reliable precursors for predicting the onset of seizures (Figs. 5, 6). Yet, our data suggest that significant pre-seizure changes, if any, depended on the brain state: that is, seizures under an identical brain state were likely to be followed by similar transient network properties (Table 4).

The duration of the sliding window, w, and the threshold, T, that were used to transform $\gamma_{ij}^{\max}$ into a_{ij} are ad hoc parameters in the current study. The selected length of w is a tradeoff between stationarity of analyses and temporal resolution. A long window size of 25 s was adopted in our analyses to extract reliable functional networks; shortening w, on the other hand, might enhance sensitivity to precursors prior to seizures. The structure of functional networks also substantially depends on T (Fig. 2c). A large T extracts reliable functional networks, but in turn results in a sparse graph, for which network properties cannot be properly characterized. For example, to estimate small-world properties, $\langle k_i \rangle$ should be larger than $\ln(n)$ [e.g., for $n = 120$ (patient #2), $\langle k_i \rangle$ should be greater than 4.79] [25]. On the other hand, if T is small, the functional networks are likely to contain unimportant, distracting links. The blending probability was thus introduced in the present analyses as a practical, well-balanced solution to objectively determine the T at which the network properties in the pre-seizure period become most distinct from those in an interictal state (Fig. 3). The adequacy of the range of thus-derived values for T (i.e., 6–14) confirmed the appropriateness of this method. Furthermore, large L and C during seizure were consistent with existing reports [20, 21], verifying that our analysis is able to adequately extract state-dependent network properties.

The current study demonstrated only limited effectiveness in terms of seizure prediction, but helps give direction for future studies. First, the study suggests that consideration of brain states may be required for seizure prediction. Limited success to date despite extensive attempts to predict seizures may be partly the result of overlooking the possibility that many precursors are state-dependent. Mormann et al. [14, 15] found relatively consistent seizure precursors with anticipation time on the order of 1 h. Therefore, identification of the presentiment state of seizure may be a vital step in seizure prediction. Second, global properties such as k_i, L and C can be used for characterizing states, but not for predicting transient shifts from pre-seizure states to ictal states. Previous studies also reported poor predictive abilities of global properties via either graph theory [20, 21] or other multi-variate measures [18]. Instead, local synchrony between specific electrode pairs may be more useful for prediction [14, 15, 19, 26]. Furthermore, dynamic interactions of epileptic activities [27–30] with pre-determined functional networks should be

taken into account in attempts to predict the extent of seizure spreading [17, 31].

Acknowledgment This work was financially supported partly by the Ministry of Health, Labour and Welfare of Japan (Grant for Comprehensive Research on Disability, Health and Welfare; H23-Nervous and Muscular-General-003).

Conflict of interest The authors do not have any conflict of interest to be declared.

References

1. Elger CE (2001) Future trends in epileptology. Curr Opin Neurol 14(2):185–186
2. Theodore WH, Fisher RS (2004) Brain stimulation for epilepsy. Lancet Neurol 3(2):111–118
3. Osorio I, Frei MG, Sunderam S, Giftakis J, Bhavaraju NC, Schaffner SF, Wilkinson SB (2005) Automated seizure abatement in humans using electrical stimulation. Ann Neurol 57(2):258–268
4. Morrell M (2006) Brain stimulation for epilepsy: can scheduled or responsive neurostimulation stop seizures? Curr Opin Neurol 19(2):164–168
5. Mormann F, Andrzejak RG, Elger CE, Lehnertz K (2007) Seizure prediction: the long and winding road. Brain 130(Pt 2):314–333
6. Rogowski Z, Gath I, Bental E (1981) On the prediction of epileptic seizures. Biol Cybern 42(1):9–15
7. Siegel A, Grady CL, Mirsky AF (1982) Prediction of spike-wave bursts in absence epilepsy by EEG power-spectrum signals. Epilepsia 23(1):47–60
8. Salant Y, Gath I, Henriksen O (1998) Prediction of epileptic seizures from two-channel EEG. Med Biol Eng Comput 36(5):549–556
9. Iasemidis LD, Sackellares JC, Zaveri HP, Williams WJ (1990) Phase space topography and the Lyapunov exponent of electrocorticograms in partial seizures. Brain Topogr 2(3):187–201
10. Martinerie J, Adam C, Le Van Quyen M, Baulac M, Clemenceau S, Renault B, Varela FJ et al (1998) Epileptic seizures can be anticipated by non-linear analysis. Nat Med 4(10):1173–1176
11. Le Van Quyen M, Martinerie J, Navarro V, Boon P, D'Have M, Adam C, Renault B, Varela F, Baulac M (2001) Anticipation of epileptic seizures from standard EEG recordings. Lancet 357(9251):183–188
12. D'Alessandro M, Esteller R, Vachtsevanos G, Hinson A, Echauz J, Litt B (2003) Epileptic seizure prediction using hybrid feature selection over multiple intracranial EEG electrode contacts: a report of four patients. IEEE Trans Biomed Eng 50(5):603–615
13. D'Alessandro M, Vachtsevanos G, Esteller R, Echauz J, Cranstoun S, Worrell G, Parish L, Litt B (2005) A multi-feature and multi-channel univariate selection process for seizure prediction. Clin Neurophysiol 116(3):506–516
14. Mormann F, Kreuz T, Andrzejak RG, David P, Lehnertz K, Elger CE (2003) Epileptic seizures are preceded by a decrease in synchronization. Epilepsy Res 53(3):173–185
15. Mormann F, Kreuz T, Rieke C, Andrzejak RG, Kraskov A, David P, Elger CE, Lehnertz K (2005) On the predictability of epileptic seizures. Clin Neurophysiol 116(3):569–587
16. Esteller R, Echauz J, D'Alessandro M, Worrell G, Cranstoun S, Vachtsevanos G, Litt B (2005) Continuous energy variation during the seizure cycle: towards an on-line accumulated energy. Clin Neurophysiol 116(3):517–526
17. Wendling F, Bartolomei F, Bellanger JJ, Bourien J, Chauvel P (2003) Epileptic fast intracerebral EEG activity: evidence for spatial decorrelation at seizure onset. Brain 126(Pt 6):1449–1459
18. Schindler K, Leung H, Elger CE, Lehnertz K (2007) Assessing seizure dynamics by analysing the correlation structure of multichannel intracranial EEG. Brain 130(Pt 1):65–77
19. Kuhlmann L, Freestone D, Lai A, Burkitt AN, Fuller K, Grayden DB, Seiderer L, Vogrin S, Mareels IM, Cook MJ (2010) Patient-specific bivariate-synchrony-based seizure prediction for short prediction horizons. Epilepsy Res 91(2–3):214–231
20. Ponten SC, Bartolomei F, Stam CJ (2007) Small-world networks and epilepsy: graph theoretical analysis of intracerebrally recorded mesial temporal lobe seizures. Clin Neurophysiol 118(4):918–927
21. Schindler KA, Bialonski S, Horstmann MT, Elger CE, Lehnertz K (2008) Evolving functional network properties and synchronizability during human epileptic seizures. Chaos 18(3):033119
22. Lehnertz K (1999) Non-linear time series analysis of intracranial EEG recordings in patients with epilepsy—an overview. Int J Psychophysiol 34(1):45–52
23. Kreuz T, Andrzejak RG, Mormann F, Kraskov A, Stogbauer H, Elger CE, Lehnertz K, Grassberger P (2004) Measure profile surrogates: a method to validate the performance of epileptic seizure prediction algorithms. Phys Rev E Stat Nonlin Soft Matter Phys 69(6 Pt 1):061915
24. Navarro V, Martinerie J, Le Van Quyen M, Baulac M, Dubeau F, Gotman J et al (2005) Seizure anticipation: do mathematical measures correlate with video-EEG evaluation? Epilepsia 46(3):385–396
25. Watts DJ, Strogatz SH (1998) Collective dynamics of 'small-world' networks. Nature 393(6684):440–442
26. Winterhalder M, Schelter B, Maiwald T, Brandt A, Schad A, Schulze-Bonhage A, Timmer J (2006) Spatio-temporal patient-individual assessment of synchronization changes for epileptic seizure prediction. Clin Neurophysiol 117(11):2399–2413
27. Bragin A, Engel J Jr, Wilson CL, Fried I, Mathern GW (1999) Hippocampal and entorhinal cortex high-frequency oscillations (100–500 Hz) in human epileptic brain and in kainic acid-treated rats with chronic seizures. Epilepsia 40(2):127–137
28. Huberfeld G, Menendez de la Prida L, Pallud J, Cohen I, Le Van Quyen M, Adam C, Clemenceau S, Baulac M, Miles R et al (2011) Glutamatergic pre-ictal discharges emerge at the transition to seizure in human epilepsy. Nat Neurosci 14(5):627–634
29. Truccolo W, Donoghue JA, Hochberg LR, Eskandar EN, Madsen JR, Anderson WS, Brown EN, Halgren E, Cash SS (2011) Single-neuron dynamics in human focal epilepsy. Nat Neurosci 14(5):635–641
30. Yaari Y, Beck H (2002) "Epileptic neurons" in temporal lobe epilepsy. Brain Pathol 12(2):234–239
31. Lago-Fernandez LF, Huerta R, Corbacho F, Siguenza JA et al (2000) Fast response and temporal coherent oscillations in small-world networks. Phys Rev Lett 84(12):2758–2761

See the corresponding editorial in this issue, pp 1219–1220.

J Neurosurg 116:1221–1225, 2012

Delayed complication after Gamma Knife surgery for mesial temporal lobe epilepsy

Clinical article

Kenichi Usami, M.D.,[1] Kensuke Kawai, M.D., Ph.D.,[1] Tomoyuki Koga, M.D., Ph.D.,[1] Masahiro Shin, M.D., Ph.D.,[1] Hiroki Kurita, M.D., Ph.D.,[2] Ichiro Suzuki, M.D., Ph.D.,[3] and Nobuhito Saito, M.D., Ph.D.[1]

[1]Department of Neurosurgery, The University of Tokyo Hospital, Tokyo; [2]Department of Cerebrovascular Surgery, Saitama Medical University International Medical Center, Saitama; and [3]Department of Neurosurgery, Japanese Red Cross Medical Center, Tokyo, Japan

Object. Despite the controversy over the clinical significance of Gamma Knife surgery (GKS) for refractory mesial temporal lobe epilepsy (MTLE), the modality has attracted attention because it is less invasive than resection. The authors report long-term outcomes for 7 patients, focusing in particular on the long-term complications.

Methods. Between 1996 and 1999, 7 patients with MTLE underwent GKS. The 50% marginal dose covering the medial temporal structures was 18 Gy in 2 patients and 25 Gy in the remaining 5 patients.

Results. High-dose treatment abolished the seizures in 2 patients and significantly reduced them in 2 others. One patient in this group was lost to follow-up. However, 2 patients presented with symptomatic radiation necrosis (SRN) necessitating resection after 5 and 10 years. One patient who did not need necrotomy continued to show radiation necrosis on MRI after 10 years. One patient died of drowning while swimming in the sea 1 year after GKS, before seizures had disappeared completely.

Conclusions. High-dose treatment resulted in sufficient seizure control but carried a significant risk of SRN after several years. Excessive target volume was considered as a reason for delayed necrosis. Drawbacks such as a delay in seizure control and the risk of SRN should be considered when the clinical significance of this treatment is evaluated. *(http://thejns.org/doi/abs/10.3171/2012.2.JNS111296)*

Key Words • **Gamma Knife surgery** • **mesial temporal lobe epilepsy** • **delayed complication** • **symptomatic radiation necrosis** • **oncology**

Accumulating evidence suggests that surgical treatment for intractable MTLE achieves favorable outcomes,[6,20,23] and medial temporal lobectomy is generally the first choice for the treatment of intractable MTLE. However, as a complete elimination of the complications associated with craniotomy is difficult, GKS has attracted attention as an alternative to craniotomy. Gamma Knife surgery for AVMs,[10] glioma,[5,18,19] and other intracranial lesions associated with epilepsy has shown antiepileptic effects, which have since been applied in cases of intractable MTLE. Gamma Knife surgery for MTLE was first performed by Régis et al.,[16] and it began to be used at several other facilities in the late 1990s.[2,4,11,15,17,21] Recently, a multicenter randomized study with a 3-year follow-up demonstrated that GKS offered seizure remission rates comparable to those of open surgery,[1] while a second report with 8 years of follow-up failed to demonstrate that GKS successfully controls seizures over the long term.[22] The clinical significance of GKS for MTLE remains undetermined, and its role in the treatment of MTLE needs to be further evaluated for efficacy and safety.

In this article, we report the long-term outcomes of 7 patients who underwent GKS for MTLE, and we consider the potential for the development of delayed complications.

Abbreviations used in this paper: AVM = arteriovenous malformation; CPS = complex partial seizure; GKS = Gamma Knife surgery; MTLE = mesial temporal lobe epilepsy; SRN = symptomatic radiation necrosis.

Methods

Patient Population

Our protocol for GKS in patients with intractable epilepsy was approved by the ethics committee of the University of Tokyo in August 1996.[11] Between December

1996 and August 1999, 7 patients were diagnosed with intractable MTLE; 6 patients had hippocampal sclerosis, and 1 patient had cavernous hemangioma. All patients underwent presurgical evaluations that included CT scanning, MRI, ictal and interictal SPECT, FDG-PET, and simultaneous video-electroencephalography recording. The side of epileptogenic focus could not be determined in 3 of the 7 patients after these noninvasive examinations, including a patient with interictal spikes from the contralateral side of the lesion on MRI and 2 patients with bilateral hippocampal accumulation in ictal SPECT. Thus, these patients underwent the placement of bilateral intracranial electrodes, and the side of epileptic focus was confirmed (Table 1).

Gamma Knife Surgery Protocol

The 50% isodose line covered the amygdala, hippocampal head and body, most of the parahippocampal gyrus, and the entorhinal cortex (Fig. 1). The marginal dose at 50% isodose was 18 Gy in the first 2 cases (low-dose group). Eight isocenters with an 8-mm collimator and 3 isocenters with a 14-mm collimator were used in the patient in Case 1, and 8 isocenters with an 8-mm collimator and 4 isocenters with a 14-mm collimator were used in the patient in Case 2. Because the low-dose protocol was not effective in these 2 patients, the marginal dose was increased to 25 Gy, and 4 isocenters with an 18-mm collimator were used in the remaining 5 patients (high-dose group). We used the radiosurgical planning software KULA (Elekta Instruments) until September 1998 (in Cases 1–4); thereafter, GammaPlan (Elekta Instruments) was used (in Cases 5–7).

Follow-Up

After GKS, all patients were observed for seizure frequency and complications, and postoperative changes were evaluated by periodic MRI examinations.

Results

Low-Dose Group

The patients in the low-dose GKS group (Cases 1 and 2) had no seizure reduction by 30 months (Case 1) and 16 months (Case 2). Both patients underwent an anterior medial temporal lobectomy. Each patient experienced complete seizure remission immediately after surgery. Detailed descriptions of the early low-dose group have been reported elsewhere.[11]

High-Dose Group

In the high-dose group (Cases 3–7), CPSs had disappeared in 2 patients (Cases 3 and 4) and were significantly decreased in 2 patients (Cases 5 and 7); however, the patient in Case 7 died of drowning while swimming in the sea 1 year after GKS. One patient was lost to follow-up (Case 6). Two patients who became CPS free required a craniotomy due to SRN after long-term recovery following GKS.

The patient in Case 3 developed mild headache 6 months after GKS. A small area of edema and slight contrast enhancement in the temporal lobe were noted on MRI 10 months after GKS. The patient was subsequently prescribed steroids to treat the persistent headache and for the enlargement of the enhanced lesion with diffuse edema on MRI. After steroid administration, the enhanced lesion and edema did not expand, but it also did not disappear. After 5 years, the patient developed generalized convulsive seizures, and MRI showed that necrosis and diffuse edema remained (Fig. 2). The patient underwent a necrotomy, which abolished her seizures completely. The resected specimen showed radiation necrosis without malignant tumor cells.

The patient in Case 4 presented with gait disturbance 8 years after GKS, and MRI revealed hydrocephalus, augmentation of necrosis, and extension of edema. At this time she underwent ventriculoperitoneal shunt placement, which improved her hydrocephalus. However, necrosis and edema continued to expand, and a necrotomy was performed 2 years after ventriculoperitoneal shunt placement (Fig. 3). She became seizure free after surgery. The resected specimen revealed radiation necrosis without malignant tumor cells.

The patient in Case 5 has not reported about symptoms caused by an increase in intracranial pressure associated with SRN after GKS. However, the lesion, which enhanced on Gd administration, cyst formation, and perifocal edema were still noted on the MRI studies 10 years after GKS (Fig. 4). At present, the patient has a few seizure attacks a year.

TABLE 1: Patient characteristics*

Case No.	Age (yrs), Sex	FC	Intracranial Electrode	Age at Seizure Onset (yrs)	MRI Atrophy	Hypometabolism	Seizure Origin on Video-EEG	GKS Side
1	31, F	yes	yes	6	rt	no laterality	rt	rt
2	22, M	yes	no	9	rt	rt	rt	rt
3	30, F	yes	yes	22	lt	bilat	lt	lt
4	66, F	no	no	45	rt	rt	rt	rt
5	33, F	yes	yes	18	rt	rt	rt	rt
6	24, F	no	no	15	rt	rt	rt	rt
7	41, M	yes	no	12	rt	rt	rt	rt

* EEG = electroencephalography; FC = febrile convulsion.